Role of defects in the carrier-tunable topological-insulator (Bi$_{1-x}$Sb$_x$)$_2$Te$_3$ thin films

Kane L. Scipioni,[1] Zhenyu Wang,[1,*] Yulia Maximenko,[1] Ferhat Katmis,[2] Charlie Steiner,[1] and Vidya Madhavan[1,†]

[1]*Department of Physics, University of Illinois Urbana-Champaign, Urbana, Illinois 61801, USA*
[2]*Department of Physics, Massachusetts Institute of Technology, Cambridge, Massachusetts 02139, USA*

Alloys of Bi$_2$Te$_3$ and Sb$_2$Te$_3$ [(Bi$_{1-x}$Sb$_x$)$_2$Te$_3$] have played an essential role in the exploration of topological surface states, allowing us to study phenomena that would otherwise be obscured by bulk contributions to conductivity. Despite intensive transport and angle resolved photoemission (ARPES) studies, important questions about this system remain unanswered. For example, previous studies reported the chemical tuning of the Fermi level to the Dirac point by controlling the Sb:Bi composition ratio, but the optimum ratio varies widely across various studies. Moreover, it is unclear how the quasiparticle lifetime is affected by the disorder resulting from Sb/Bi alloying. In this work, we use scanning tunneling microscopy and spectroscopy to study the electronic structure of epitaxially grown (Bi,Sb)$_2$Te$_3$ thin films at the nanoscale. We study Landau levels (LLs) to determine the effect of disorder on the quasiparticle lifetime as well as the position of the Dirac point with respect to the Fermi energy. A plot of the LL peak widths shows that despite the intrinsic disorder, the quasiparticle lifetime is not significantly degraded. We further determine that the ideal Sb concentration to place the Fermi energy to within a few meV of the Dirac point is $x \sim 0.7$, but that postannealing temperatures can have a significant effect on the crystallinity and Fermi level position. Specifically, high postgrowth annealing temperature can result in better crystallinity and surface roughness, but also produces a larger Te defect density which adds n-type carriers. Finally, in combination with quasiparticle interference imaging, the dispersion is revealed over a large energy range above the Fermi energy, in a regime inaccessible to ARPES. Interestingly, the surface state dispersion for the $x \sim 0.7$ sample shows great similarity to pristine Bi$_2$Te$_3$. This work provides microscopic information on the role of disorder and composition in determining carrier concentration, surface state dispersion, and quasiparticle lifetime in (Bi$_{1-x}$Sb$_x$)$_2$Te$_3$.

I. INTRODUCTION

The V-VI semiconductor class of compounds contain several prototypical 3D topological insulators (TI), namely Bi$_2$Se$_3$, Bi$_2$Te$_3$, and Sb$_2$Te$_3$, which possess gapless spin-momentum locked surface states and an insulating bulk [1–3]. While the existence of topological surface states has been verified [4–10], difficulties remain in isolating the effects of the topological states from the bulk contribution to the total conductance, which is required for further applications in electronic devices. This is attributed to inherent bulk conductivity caused by intrinsic defect doping in the binary compounds [11,12]. Currently, the best way to reduce bulk carriers in Bi$_2$Te$_3$ is to alloy it with Sb$_2$Te$_3$ [13–17]. The rationale for this is that mixing Bi$_2$Te$_3$, which is plagued mostly by n-type Te vacancies [11], with Sb$_2$Te$_3$, which mostly contains p-type antisite impurities [11,12], using appropriate compositional ratios, will result in a net zero bulk carrier density. This method has led to the successful observations of the quantum anomalous Hall effect (QAHE) [18] and chiral Majorana modes [19] in the thin films.

Despite these successes, a fine-tuning of the chemical potential in such (Bi$_{1-x}$Sb$_x$)$_2$Te$_3$ (BST) thin films continues to remain an issue and the optimum ratio varies widely across different studies [13,15,20]. Moreover, the properties of Dirac quasiparticles in BST have not been fully understood yet. The QAHE observation, for instance, is limited to very low temperatures (< 1 K), a problem attributed to doping inhomogeneities and local chemical potential variations [21]. In fact, due to the random alloying of Bi and Sb atoms, there is significant disorder in this system, which may dramatically modify the electronic structure. In other systems, it has been shown that Landau quantization may be suppressed and eventually disappear with increasing disorder [22], which directly reflects the decrease in quasiparticle lifetime with disorder. In this context, it is important to reveal the electronic structure at nanoscale, something that has not been done yet in BST. In this study, we use bulk and nanoscale characterization techniques to obtain the nanoscale morphology as well as the electronic structure of BST thin films. The composition and nanoscale structure of the thin films were determined with x-ray photoelectron spectroscopy (XPS) and scanning tunneling microscopy/spectroscopy (STM/S), and the electronic structure was determined by Landau level spectroscopy and quasiparticle interference imaging.

II. EXPERIMENTAL DETAILS

BST thin films were grown using a home-built molecular beam epitaxy (MBE) system. The films were grown on C-plane oriented Al$_2$O$_3$ substrates, which were baked at
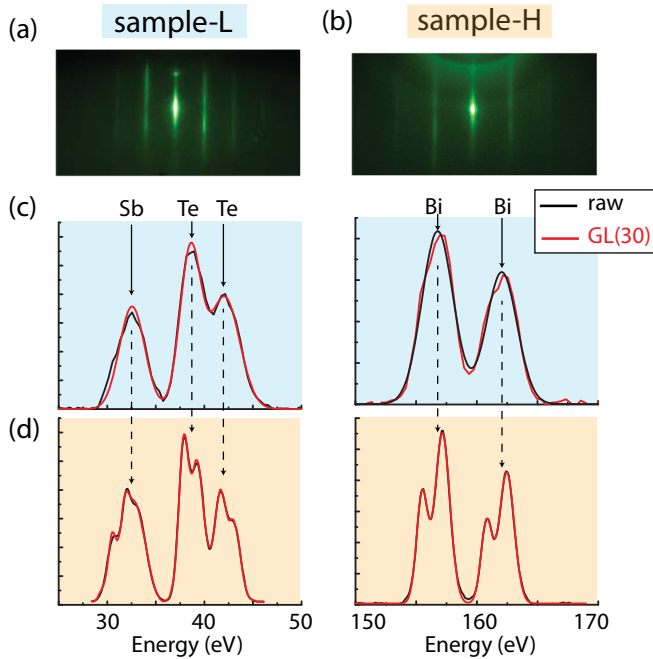
*zywang@illinois.edu
†vm1@illinois.edu

FIG. 1. (a),(b) RHEED patterns of sample-L (a) and sample-H (b). (c),(d) The background subtracted XPS counts and the fitted mixed Gaussian-Lorentzian peaks from the sample-L (c) and the sample-H (d). The arrows indicate which elements are associated with each set of electron photoemission peaks. The peaks are split in energy for the sample-H data because the scan step size in energy was smaller, but does not measurably affect the ratio of integrated counts.

FIG. 2. (a),(c) 400×400 nm and 10×10 nm (inset) STM topographic images of sample-L (a) and sample-H (c). Images were acquired at $V_S = 0.6$ V, $I_t = 50$ pA for both large scans; 0.1 V, 550 pA for inset of (a); 0.1 V, 200 pA for inset of (c). (b),(d) Typical dI/dV spectra of sample-L and sample-H, respectively.

1000 °C prior to insertion to the MBE system with a base pressure of 4×10^{-10} Torr. The growth was done by coevaporation of Bi (99.9999%), Sb (99.9999%), and Te (99.9999%) from standard single filament (Bi,Sb) and dual filament (Te) effusion cells. The substrates were held at a temperature of 180–200 °C during the growth. Typical growth rates used were 0.3–0.4 nm/min. In this paper, we compare and contrast the properties of two samples that we label sample-L and sample-H. The flux ratios were Sb:Bi = 1.36:1 and Te:(Sb,Bi)=2.1:1 for sample-L and Sb:Bi=1.57:1 and Te:(Sb,Bi)=2.2:1 for sample-H.

Directly after growth, the films were transferred to a low temperature scanning tunneling microscope using a custom vacuum shuttle system to prevent environmental exposure. STM/S measurements were performed at 4 K. In the measurements, electrochemically etched tungsten tips were used. The tunneling spectra were acquired using the lock-in technique with ac modulation about 3 mV at 987.5 Hz.

III. RESULTS AND DISCUSSION

First, we show the RHEED patterns of two nominally similar thins films of BST, postgrowth annealed at two different temperatures, 220 °C (sample-L) or 300 °C (sample-H) in Figs. 1(a) and 1(b). Both RHEED images indicate crystalline two-dimensional film growth. The slightly sharper streaks of the RHEED patterns of sample-H potentially signify better crystallinity. This will be confirmed later when we discuss STM data on these samples.
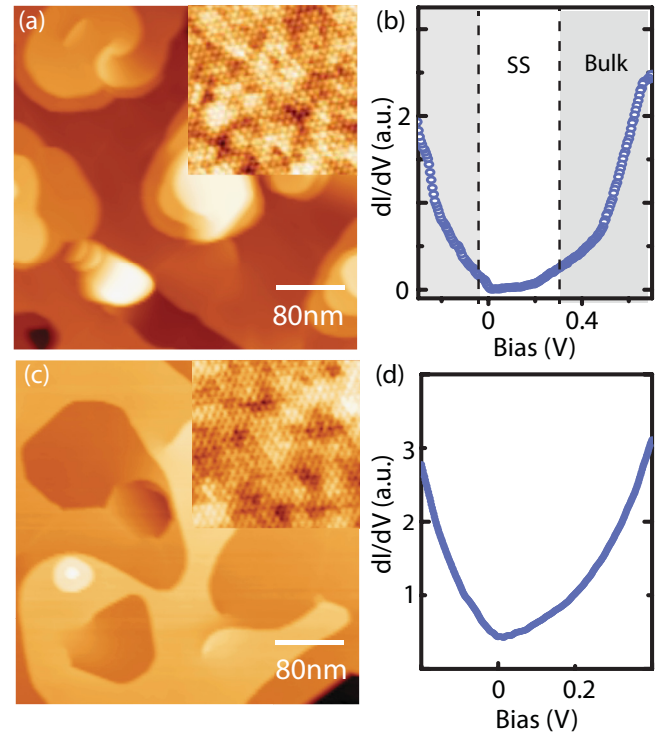
We then determine values for Sb:Bi composition ratio, x, of our films. The composition was controlled by setting the effusion flux ratio of Bi and Sb during growth. However, setting a particular flux ratio is not sufficient to determine the actual composition. So, we determine the chemical composition using *ex situ* XPS measurements. A Physical Electronics PHI 5400 instrument with a Mg source was used to obtain XPS spectra as shown in Figs. 1(c) and 1(d). Quantitative information was obtained by analyzing Te $4d$, Bi $4f$, and Sb $4d$ emission lines. The spectra were calibrated using one of $4d$ emission lines of Te and the peaks were fit with a Gaussian-Lorentzian product with the 30% contribution of the Lorentzian factor [GL(30)]. Quantitative information was obtained by integrating the fitted signal for all the chemical states of the chosen emission lines for each of the three elements and normalizing it with the instrument independent relative sensitivity factor (RSF), which was taken from the standard elemental library of the XPS analysis software CasaXPS. The resulting compositional fractions were $x = 0.68$ for sample-L and $x = 0.71$ for sample-H. For Te compositions, the Te:(Bi,Sb) ratios were 1.51 for the sample-L and 1.16 for the sample-H, indicating a Te deficiency in the latter.

To characterize the morphology of the films, large scale (400×400 nm) topographic images of sample-L and sample-H are shown in Figs. 2(a) and 2(c). The step height between terraces is about 1 nm, corresponding to one quintuple layer. The atomic-resolution images are shown as insets and the lattice constant is about 0.435 nm. Zooming in, we see that

the topography shows variations at the nanometer length scale, which can be attributed to the random Bi/Sb alloying. Unlike the binary compounds [12,23], it is very difficult to identify individual defects and we cannot directly count the number of Te vacancies in the topographies of BST films. One possible reason is that the dominant Te vacancy lies in the middle of the quintuple layer [23] and the random Bi/Sb alloy in the upper layer makes them invisible in the topography.

Though the RHEED patterns indicated reasonable crystallinity, grain boundaries and screw dislocations were observed in topographic images of both samples. The microscopic roughness can be characterized by the height of the islands within a certain area. From Figs. 2(a) and 2(c), we find that the root-mean-squared roughness of sample-L is 1.2 nm and for sample-H is 0.7 nm, indicating that the postanneal temperature affects roughness at the microscale.

Next, we characterize the electronic structure and measure the energy of the Dirac point (DP) with respect to the Fermi level. The $dI/dV(r, eV)$ spectra, which measure the local density of states (LDOS), are shown in Figs. 2(b) and 2(d). For sample-L, the LDOS is strongly suppressed from -20 meV to 260 meV, resulting in a bulk gap about 280 meV. The positions of the DP, determined by the minima of LDOS, seems close to Fermi level for both samples. However, this method is fraught with problems because the tip's density of states can influence the shape of the dI/dV spectra, shifting the minimum away

from the Dirac point. Additionally, the contribution of the surface states to the total density of states may be obscured by bulk bands. For example, this happens in Bi_2Te_3 because the DP is at a lower energy than the top of the bulk valence bands. A more accurate and reliable method to identify the position of the DP is to use Landau level spectroscopy.

In the presence of a magnetic field, electrons fall into quantized cyclotron orbits called Landau levels (LLs), which appear as peaks in the dI/dV spectra. The energies of these states disperse with respect to magnetic field strength. For massless Dirac fermions, the dispersion is

$$E_n = E_D + \text{sgn}(n) v_F \sqrt{2eB\hbar|n|}, \qquad (1)$$

where E_D is the Dirac point energy, v_F is the Fermi velocity, n is the Landau level index, and B is the field strength. Assuming the usual g factor of 2, the term resulting from the electron g factor is negligible and has been ignored in Eq. (1). In fact, as we will see later, our data are reasonably consistent with this assumption. An important aspect of Eq. (1) is that we expect to see a nondispersing peak exactly at the DP, and the energy can be identified with accuracy.

dI/dV spectra were acquired along a 15 nm line cut for both samples at various perpendicular magnetic fields ranging from 0 T to 7.5 T. The line cut averaged spectra are shown in Figs. 3(a) and 3(c). To remove the background, the 0 T
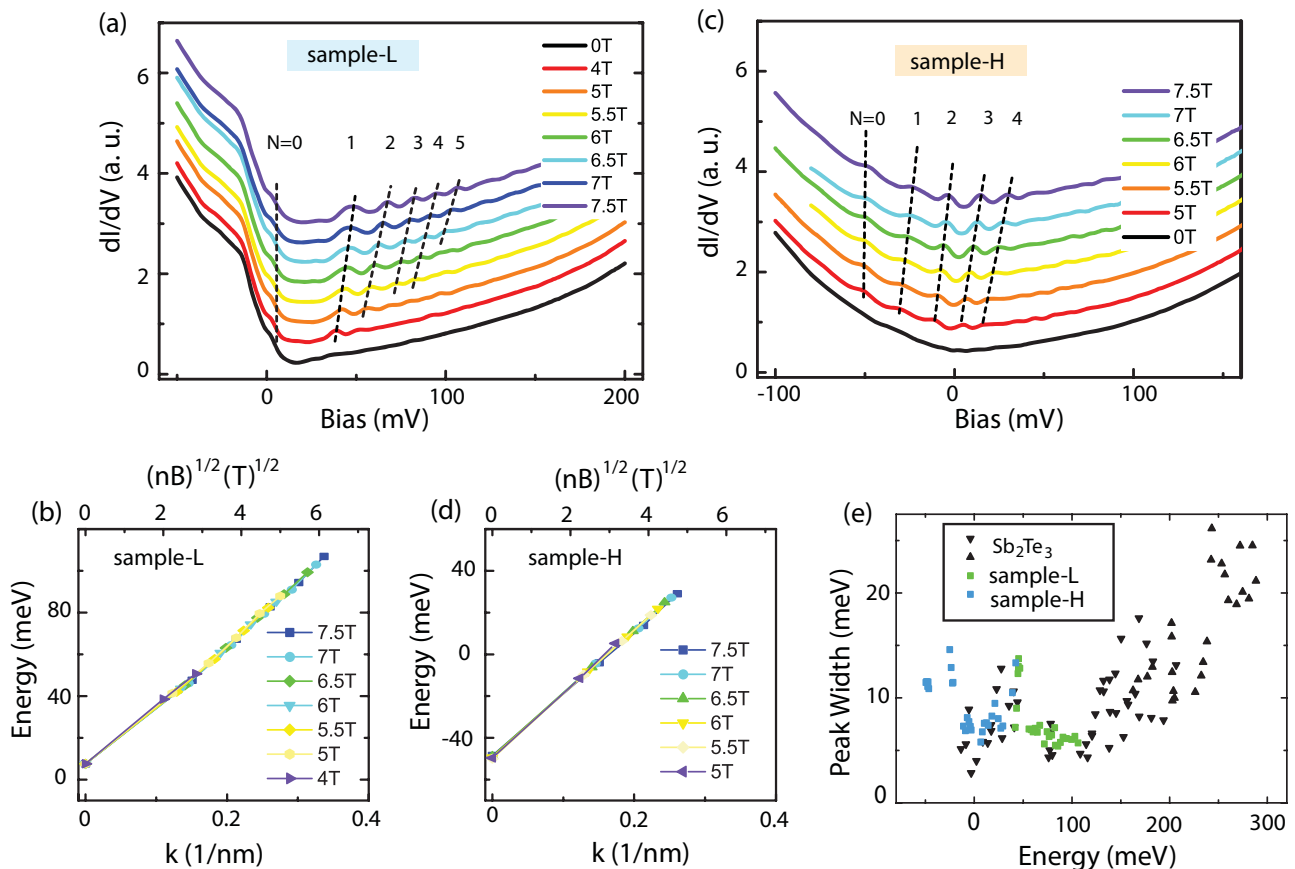

FIG. 3. (a),(c) Landau level spectroscopy for sample-L (a) and sample-H (c). (b),(d) Dispersion of surface state for the sample-L (b) and sample-H (d). Linear fit to Eq. (1) gives $E_D = 6$ mV for L and $E_D = -48$ mV for H. Both samples have a Fermi velocity $v_F = 4.4 \times 10^5$ m/s. (e) Full width at half maximum for each LL peaks plotted as a function of energy for sample L, H, and Sb_2Te_3 [25,26].
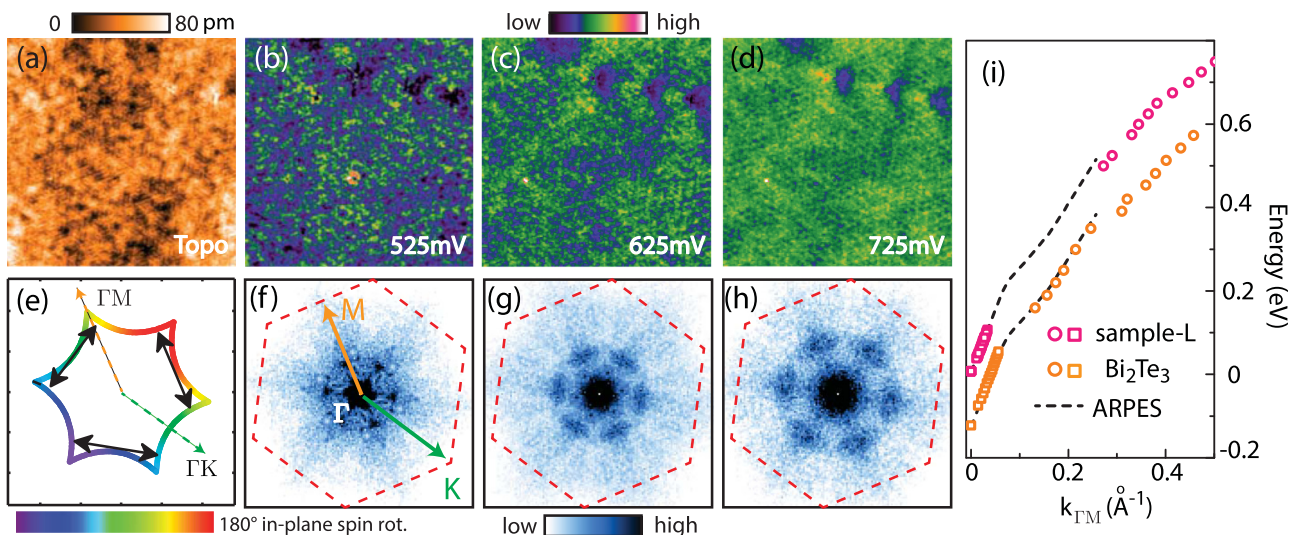
FIG. 4. (a) Topography of the sample-L (40 nm × 40 nm). (b)–(d) dI/dV maps of the field of view as (a) with different energies. (e) Schematic constant energy contours in momentum space. The solid arrows denote possible scattering vectors. (f)–(h) FFT of the dI/dV maps shown in (b)–(d), respectively. The first Brillouin zone is denoted with red dash lines. (i) A summary of the dispersion of BST films and Bi$_2$Te$_3$. The orange open squares and circles are reproduced from previous LL and QPI measurements, respectively [24]. The dotted lines are based on previous angle-resolved photoemission spectroscopy studies of Bi$_2$Te$_3$ but rigidly shifted to match the dispersion here [4].

spectrum was subtracted from spectra at other fields. LL peak positions were obtained by fitting the peaks to Lorenzian functions. The resulting LL peak energies are plotted in Figs. 3(b) and 3(d) with respect to $\sqrt{nB}$, which can then be converted into momentum using a semiclassical approximation. Since near E$_D$ the Dirac cone is isotropic, the magnitude of the momentum vector can be obtained by

$$k_n = \sqrt{\frac{2eB|n|}{\hbar}}. \qquad (2)$$

Fitting the peak positions to Eq. (1) yields a DP energy of 6 mV for sample-L and −48 mV for sample-H. The Fermi velocity obtained from both fits is 4.4×10^5 m/s. This value is consistent with previous measurements of the Fermi velocity measured for Bi$_2$Te$_3$ and Sb$_2$Te$_3$.

Furthermore, the energy dependence of the quasiparticle lifetime can be extracted from the peak width of each LL by the fitting. The results for both sample L and H, together with those obtained on Sb$_2$Te$_3$ [25,26], are plotted in Fig. 3(e). In BST samples, regarding the random Sb/Bi alloying, there can be significant disorder which may broaden the LL peaks [22]. However, we find here that the peak width and its energy dependence in BST are almost identical for the Sb$_2$Te$_3$ samples. While the random alloying leads to electronic inhomogeneity, the disorder generated does not lead to a degradation of the quasiparticle lifetime. Such protection of the surface state lifetime was also observed in the topological crystalline insulator alloy Pb$_{1-x}$Sn$_x$Se [27]. To understand the effect of alloying on the quasiparticle lifetime requires further studies.

To confirm the unique scattering properties of the topological surface states, and obtain more information on the dispersion, we perform quasiparticle interference (QPI) measurements on sample-L. In QPI measurements, the spatial modulations in differential conductance maps are recorded and then Fourier transformed to extract scattering vectors connecting electronic states in momentum space. In Figs. 4(c)

and 4(d), we summarize the $dI/dV(r, eV)$ maps from 500 mV to 800 mV, which exhibit pronounced standing wave patterns. The wavelength becomes shorter with increasing energy. The Fourier transforms after symmetrization are shown in Figs. 4(f)–4(h), and we observe patterns centered along the ΓM direction of the first Brillouin zone (red dashed lines). This ΓM scattering vector originates from the hexagonally warped Dirac cones with chiral spin texture [shown as dark solid arrows in Fig. 4(e)], and backscattering is prohibited under the protection of time-reversal symmetry [28,29]. This measurement offers direct proof of the topological nature of the surface states. In Fig. 4(i), we plot the dispersion along the ΓM direction together with the results obtained from LL measurements. To make a direct comparison with the dispersion of surface states in Bi$_2$Te$_3$, we show the results obtained in our previous STM study [24] (orange spots) and ARPES [4] (black dashed lines) in the same plot. We note here that the two black dashed lines shown are identical except that one has been offset in energy with respect to the other. As can be seen by a comparison of the dashed lines to the data, the dispersion of our BST films remains mainly unchanged, except for a Fermi level shift of ∼130 meV lower compared to pristine Bi$_2$Te$_3$.

From our measurements, we find that sample-L is very close to the optimum composition as indicated by the position of the Dirac node, which is 6 meV from the Fermi energy. On the other hand, the Fermi level of sample-H is higher than sample-L implying it is more n-doped. Since the Sb:Bi ratio of the two samples is very similar, the difference in doping cannot be attributed to the ratio. In fact, the slightly larger Sb content should in principle make sample-H more p type. Given our XPS results indicate a Te deficiency in sample-H, we attribute the electron doping in sample-H to Te vacancies which are expected to act as n-type dopants in Bi/Sb rich samples. This implies that the higher annealing temperature used for sample-H caused a reevaporation of the Te after it had been incorporated during growth.

Our results show that defects arising from the film growth conditions and the BST composition affect the Fermi level separately. Therefore, the Fermi level tuning of BST by chemical composition is not simply a matter of setting the Sb:Bi compositional ratio and depends sensitively on the postanneal temperature. Our findings explain the large variations seen in the optimum Sb:Bi ratio of thin BST films reported by different groups [13,14,16]. In the absence of substantial Te vacancies, we find that the optimum composition for placing the Fermi energy close to the DP is $x \sim 0.7$. Moreover, our findings indicate a path to obtaining ideal samples for the QAHE. Sb_2Te_3 hosts a DP clearly in the gap, far from the bulk bands, but is intrinsically p type. Compensating the p-type Sb_2Te_3 by alloying with n-type Bi_2Te_3 has been used to place the Fermi energy close to the DP, but also affects the DP by moving it closer to the conduction band. However, we demonstrated that postannealing BST can introduce n-type carriers, which can be used as a parameter to obtain a finer degree of control of the electronic properties of BST films.

IV. CONCLUSION

In summary, we have performed Landau level spectroscopy and quasiparticle interference spectroscopy, in combination with x-ray spectroscopy on BST thin films grown under different conditions. We find that Fermi energy can be placed to within a few meV of the Dirac point with Sb concentration 0.7. However, for the same Sb/Bi ratio, the Fermi level can be tuned to an energy approximately 50 meV lower simply by a higher postannealing temperature. This explains the wide variations seen in the optimum Sb/Bi ratio of the BST films reported before and provides key information to obtain a finer control of the electronic properties of BST films. We also show clear Landau quantization of the Dirac quasiparticles in magnetic fields and suppressed backscattering processes, demonstrating that the topological surface states in BST are robust against the Sb/Bi alloying disorder. Specifically, the alloying disorder does not have much effect on the width of the LL peak, leaving the origin of the short quasiparticle lifetime an open question for future study.

[1] M. Z. Hasan and C. L. Kane, Rev. Mod. Phys. **82**, 3045 (2010).

[2] X.-L. Qi and S.-C. Zhang, Rev. Mod. Phys. **83**, 1057 (2011).

[3] H. Zhang, C.-X. Liu, X.-L. Qi, X. Dai, Z. Fang, and S.-C. Zhang, Nat. Phys. **5**, 438 (2009).

[4] Y. L. Chen, J. G. Analytis, J.-H. Chu, Z. K. Liu, S.-K. Mo, X. L. Qi, H. J. Zhang, D. H. Lu, X. Dai, Z. Fang, S. C. Zhang, I. R. Fisher, Z. Hussain, and Z.-X. Shen, Science **325**, 178 (2009).

[5] Y. Xia, D. Qian, D. Hsieh, L. Wray, A. Pal, H. Lin, A. Bansil, D. Grauer, Y. S. Hor, R. J. Cava, and M. Z. Hasan, Nat. Phys. **5**, 398 (2009).

[6] D. Hsieh, Y. Xia, D. Qian, L. Wray, J. H. Dil, F. Meier, J. Osterwalder, L. Patthey, J. G. Checkelsky, N. P. Ong, A. V. Fedorov, H. Lin, A. Bansil, D. Grauer, Y. S. Hor, R. J. Cava, and M. Z. Hasan, Nature (London) **460**, 1101 (2009).

[7] T. Hanaguri, K. Igarashi, M. Kawamura, H. Takagi, and T. Sasagawa, Phys. Rev. B **82**, 081305 (2010).

[8] P. Cheng, C. Song, T. Zhang, Y. Zhang, Y. Wang, J.-F. Jia, J. Wang, Y. Wang, B.-F. Zhu, X. Chen, X. Ma, K. He, L. Wang, X. Dai, Z. Fang, X. Xie, X.-L. Qi, C.-X. Liu, S.-C. Zhang, and Q.-K. Xue, Phys. Rev. Lett. **105**, 076801 (2010).

[9] H. Beidenkopf, P. Roushan, J. Seo, L. Gorman, I. Drozdov, Y. S. Hor, R. J. Cava, and A. Yazdani, Nat. Phys. **7**, 939 (2011).

[10] Y. Okada, C. Dhital, W. Zhou, E. D. Huemiller, H. Lin, S. Basak, A. Bansil, Y.-B. Huang, H. Ding, Z. Wang, S. D. Wilson, and V. Madhavan, Phys. Rev. Lett. **106**, 206805 (2011).

[11] D. O. Scanlon, P. D. C. King, R. P. Singh, A. de la Torre, S. M. Walker, G. Balakrishnan, F. Baumberger, and C. R. A. Catlow, Adv. Mater. **24**, 2154 (2012).

[12] Y. Jiang, Y. Y. Sun, M. Chen, Y. Wang, Z. Li, C. Song, K. He, L. Wang, X. Chen, Q.-K. Xue, X. Ma, and S. B. Zhang, Phys. Rev. Lett. **108**, 066809 (2012).

[13] J. Zhang, C.-Z. Chang, Z. Zhang, J. Wen, X. Feng, K. Li, M. Liu, K. He, L. Wang, X. Chen, Q.-K. Xue, X. Ma, and Y. Wang, Nat. Commun. **2**, 574 (2011).

[14] X. He, T. Guan, X. Wang, B. Feng, P. Cheng, L. Chen, Y. Li, and K. Wu, Appl. Phys. Lett. **101**, 123111 (2012).

[15] X. He, H. Li, L. Chen, and K. Wu, Sci. Rep. **5**, 8830 (2015).

[16] L. He, X. Kou, M. Lang, E. S. Choi, Y. Jiang, T. Nie, W. Jiang, Y. Fan, Y. Wang, F. Xiu, and K. L. Wang, Sci. Rep. **3**, 3406 (2013).

[17] D. Kong, Y. Chen, J. J. Cha, Q. Zhang, J. G. Analytis, K. Lai, Z. Liu, S. S. Hong, K. J. Koski, S.-K. Mo, Z. Hussain, I. R. Fisher, Z.-X. Shen, and Y. Cui, Nat. Nanotechnol. **6**, 705 (2011).

[18] C.-Z. Chang, J. Zhang, X. Feng, J. Shen, Z. Zhang, M. Guo, K. Li, Y. Ou, P. Wei, L.-L. Wang, Z.-Q. Ji, Y. Feng, S. Ji, X. Chen, J. Jia, X. Dai, Z. Fang, S.-C. Zhang, K. He, Y. Wang, L. Lu, X.-C. Ma, and Q.-K. Xue, Science **340**, 167 (2013).

[19] Q. L. He, L. Pan, A. L. Stern, E. C. Burks, X. Che, G. Yin, J. Wang, B. Lian, Q. Zhou, E. S. Choi, K. Murata, X. Kou, Z. Chen, T. Nie, Q. Shao, Y. Fan, S.-C. Zhang, K. Liu, J. Xia, and K. L. Wang, Science **357**, 294 (2017).

[20] J. Kellner, M. Eschbach, J. Kampmeier, M. Lanius, E. Mlynczak, G. Mussler, B. Hollander, L. Plucinski, M. Liebmann, D. Grutzmacher, C. M. Schneider, and M. Markus, Appl. Phys. Lett. **107**, 251603 (2015).

[21] M. Mogi, R. Yoshimi, A. Tsukazaki, K. Yasuda, K. Kozuka, K. S. Takahashi, M. Kawasaki, and Y. Tokura, Appl. Phys. Lett. **107**, 182401 (2015).

[22] B. Dóra, Low Temp. Phys. **34**, 801 (2008).

[23] J. Dai, D. West, X. Wang, Y. Wang, D. Kwok, S.-W. Cheong, S. B. Zhang, and W. Wu, Phys. Rev. Lett. **117**, 106401 (2016).

[24] Y. Okada, W. Zhou, D. Walkup, C. Dhital, S. Wilson, and V. Madhavan, Nat. Commun. **3**, 1158 (2012).

[25] Y. Jiang, Y. Wang, M. Chen, Z. Li, C. Song, K. He, L. Wang, X. Chen, X. Ma, and Q.-K. Xue, Phys. Rev. Lett. **108**, 016401 (2012).

[26] C. Pauly, C. Saunus, M. Liebmann, and M. Morgenstern, Phys. Rev. B **92**, 085140 (2015).

[27] I. Zeljkovic, Y. Okada, M. Serbyn, R. Sankar, D. Walkup, W. Zhou, J. Liu, G. Chang, Y. Jui Wang, M. Z. Hasan, F. Chou, H. Lin, A. Bansil, L. Fu, and V. Madhavan, Nat. Mater. **14**, 318 (2015).

[28] T. Zhang, P. Cheng, X. Chen, J.-F. Jia, X. Ma, K. He, L. Wang, H. Zhang, X. Dai, Z. Fang, X. Xie, and Q.-K. Xue, Phys. Rev. Lett. **103**, 266803 (2009).

[29] L. Fu, Phys. Rev. Lett. **103**, 266801 (2009).